Alexandria Engineering Journal 91 (2024) 403–418

Contents lists available at ScienceDirect

Alexandria Engineering Journal

journal homepage: www.elsevier.com/locate/aej

Original Article

Design principle and numerical analysis for cycloidal drive considering clearance, deformation, and friction

Le Qi, Dapeng Yang, Baoshi Cao *, Zhiqi Li, Hong Liu

State Key Laboratory of Robotics and System, Harbin Institute of Technology, Xidazhi Street 92, Harbin, Heilongjiang 150001, China

ARTICLE INFO

Keywords:
Cycloidal drive
Robot drive
Contact analysis
Performance prediction
Transmission efficiency

ABSTRACT

This study proposes a clearance, deformation, and friction numerical analysis method for cycloidal drives (CDFM) to design and optimize. The proposed method considers clearance, deformation, and friction while providing high computational efficiency for multi-parameter optimization design. Performances such as accuracy, backlash, stiffness, load capacity, and efficiency can be predicted, making this method an effective solution for optimizing cycloidal drives for high-performance robots. This study conducts simulation experiments on cycloidal drives with different parameters, and the results provide valuable insights into the effects of geometric deviations, teeth numbers, and friction coefficients on the performances of cycloidal drives. This proposed method is an efficient and effective solution for modeling and simulating cycloidal drive performance, especially transmission efficiency. It provides valuable insights into designing and optimizing cycloidal drives for high-performance robots.

1. Introduction

Cycloidal drives are a high-performance precise transmission technology characterized by compact size, rigidity, high reduction ratio, and high load capacity. They have been extensively employed in various industrial fields, particularly heavy-duty machinery, mining, machine tools, and industrial robots that demand high load capacity and precision transmission [1–3]. In robotics, cycloidal drives are often utilized as RV reducers to construct robot joints with high precision, rigidity, and load capacity [4]. Moreover, recent robotic research has revealed that due to the cycloidal drive's high reduction ratio, impact resistance, and efficiency, it is also suitable for a wide range of new compliant robots, such as collaborative robots, exoskeleton robots, and legged robots [5–10].

Cycloidal drives are essentially specialized planetary transmissions that utilize a pin gear as the internal gear, cycloidal gears as the planetary gears, and a planetary carrier in the form of an eccentric shaft as the power input. Various studies have derived the ideal cycloidal gear tooth profile equation using different methods [11–13]. In an ideal cycloidal drive, all roller pins contact the cycloidal gear, and about half the roller pins bear the load. The teeth in the pin gear are typically designed as a rolling structure (roller pins) to transform the sliding friction of tooth contact into rolling friction, thereby improving transmission efficiency. However, cycloidal gear transmissions often require intentional clearance design due to manufacturing deviations, thermal deformation, lubrication, and assembly [14]. Furthermore, limitations in machining accuracy can give rise to minor geometric parameter deviations, which also lead to clearances.

Simulation modeling and analysis play a crucial role in the design of cycloidal drives. In some early studies, parameter analysis was conducted using ideal models without clearances [15,16]. More recent research has underscored the importance of clearances in the analysis of cycloidal drives and has taken into account various factors, such as the modified shape of the cycloidal drive [17], eccentricity deviation [18], output shaft deviation [19], and machining tolerances [20]. These factors can all impact the performance indicators of the drive in terms of accuracy, stiffness, load capacity, and backlash.

Compared to analyzing other performance aspects, assessing the efficiency of cycloidal drives presents greater challenges. Some studies have utilized ideal models without clearances to analyze frictional situations [15,21]. Other researchers have calculated contact forces in ideal models and estimated the number of actual meshing teeth to compute frictional losses [22]. Certain researchers have employed approximate modeling methods similar to bearing efficiency [23]. Some studies have estimated meshing efficiency to determine overall efficiency [23–25]. Due to the simplification of clearance conditions and various approxi-

* Corresponding author.
E-mail addresses: qile@hit.edu.cn (L. Qi), yangdapeng@hit.edu.cn (D. Yang), cbs@hit.edu.cn (B. Cao), lzq@hit.edu.cn (Z. Li), hong.liu@hit.edu.cn (H. Liu).

https://doi.org/10.1016/j.aej.2024.01.077
Received 10 May 2023; Received in revised form 23 December 2023; Accepted 29 January 2024
Available online 20 February 2024
1110-0168/© 2024 THE AUTHORS. Published by Elsevier BV on behalf of Faculty of Engineering, Alexandria University. This is an open access article under the CC BY-NC-ND license (http://creativecommons.org/licenses/by-nc-nd/4.0/).

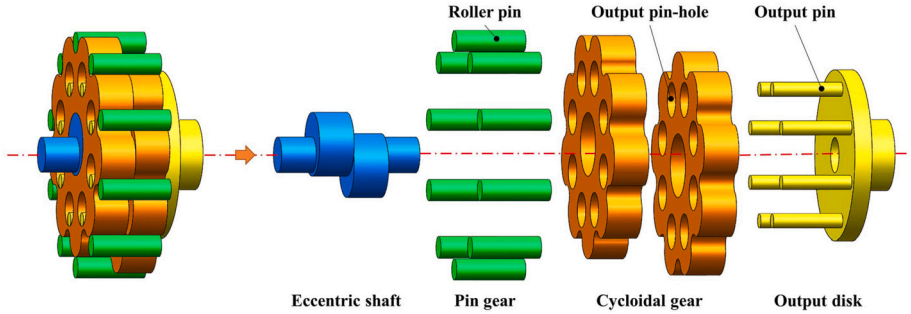


Fig. 1. The structure of a cycloidal drive.

mations, these efficiency analyses cannot accurately reflect the impact of design parameters on efficiency and are suitable only for rough efficiency estimates. On the basis of efficiency analysis methods, some researchers have also paid attention to the efficiency of special cycloid drive forms such as multi-stage cycloid drives and given application software [26,27].

In addition, many researchers have abandoned the method based on formulas and analytical solutions and turned to a more direct numerical solution method. Without considering the contact force, some researchers have proposed the transmission accuracy analysis method of cycloidal tooth profile discretization combined with the Monte Carlo method [28]; considering the contact force, many researchers choose the finite element analysis (FEA) method to solve the influence of clearances, friction, and other factors [29–31]. However, the computational efficiency of FEA is typically low, making it less suitable for optimization design and other applications that entail multi-parameter adjustments.

Traditional industrial cycloidal drive products often fail to meet the application requirements of new high-performance and flexible robots. Consequently, robotic researchers frequently design and manufacture cycloidal drives with the required performance independently, which needs detailed modeling and analysis of cycloidal drive performance, particularly their efficiency, to guide the design process. This paper proposes a quasi-static numerical modeling and analysis method (CDFM) that thoroughly accounts for clearances caused by geometric parameter deviations of each cycloidal drive component, contact deformation, and contact frictional forces between components. The method efficiently and accurately resolves the detailed contact deformation, contact forces, and contact frictional forces of each component of a given cycloidal drive, predicting key performance indicators such as transmission accuracy, stiffness, load capacity, and efficiency. Additionally, as a demonstration, this paper employs this method to simulate the cycloidal drive under various parameters.

Section 2 defines the geometric parameters of the cycloidal drive with clearances. Section 3 presents the analysis method for the cycloidal drive. Simulation experiments for cycloidal drives with different parameters are conducted in Section 4. Finally, this paper is summarized, and future work is outlined in Section 5.

2. Geometric parameters of a cycloidal drive with clearances

A typical cycloidal drive consists of four key components: an eccentric shaft (E), cycloidal gears (C), a pin gear (P), and an output disk (W), as illustrated in Fig. 1. Typically, the eccentric shaft serves as the input shaft with an eccentricity distance e. The cycloidal gear employs a curtate epicycloid tooth profile; for dynamic balance, two cycloidal gears are often symmetrically arranged. The pin gear comprises evenly spaced roller pins, with the radius and distribution radius represented as r_p and R_p, respectively. Generally, the number of teeth on the cycloidal gear, denoted by z_c, conforms to the relationship $z_p = z_c + 1$, where z_p denotes the number of roller pins on the pin gear. The output

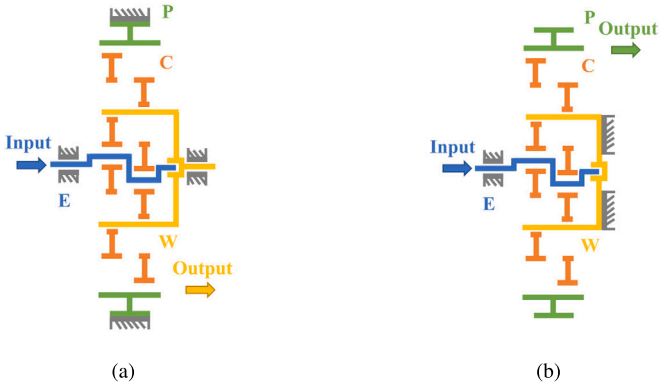


Fig. 2. (a) Configuration A, and (b) Configuration B.

disk, which transmits the rotational motion of the cycloidal gear, can assume various designs. A widely adopted configuration is the output pins structure, where the pin-holes (radius r_{wh}) on the cycloidal gear align with the same distribution radius R_{wh} as the output pins (radius r_w) on the output disk. The number of the output pins is given by z_w, satisfying

$$r_{wh} - r_w = e. \tag{1}$$

The cycloidal drive's input speed and output speed are denoted by ω_{in} and ω_{out}, respectively. In practical applications, the output disk is not always used as the power output. When the cycloidal drive is configured with configuration A, "pin gear fixed, output disk outputs" (shown in Fig. 2(a)), the theoretical transmission ratio of the cycloidal drive is:

$$I_{ew} = \frac{\omega_{in}}{\omega_{out}} = \frac{-z_c}{z_p - z_c} = -z_c. \tag{2}$$

When the cycloidal drive is configured with configuration B, "output disk fixed, pin gear outputs" (shown in Fig. 2(b)), the theoretical transmission ratio of the cycloidal drive is:

$$I_{ep} = \frac{\omega_{in}}{\omega_{out}} = \frac{z_p}{z_p - z_c} = z_p. \tag{3}$$

It should be noted that this study focuses on configuration B, which is the same configuration used in previous work [24]. The methods and conclusions in this study also apply to configuration A, and the two configurations are interchangeable.

In Fig. 3, the bearings in the cycloidal drive are simplified, the radius of the input shaft is denoted by r_e, and the equivalent bearing radius of the eccentric shaft in contact with the cycloidal gear is denoted by r_{ec}. The curve of the cycloidal gear can be obtained by solving the envelope motion of the pin gear teeth using the gear meshing principle [32].

The actual geometrical parameters of the cycloidal drive usually deviate from the theoretical values, leading to clearances, and such deviations are present in each component. Each pair of contacting com-

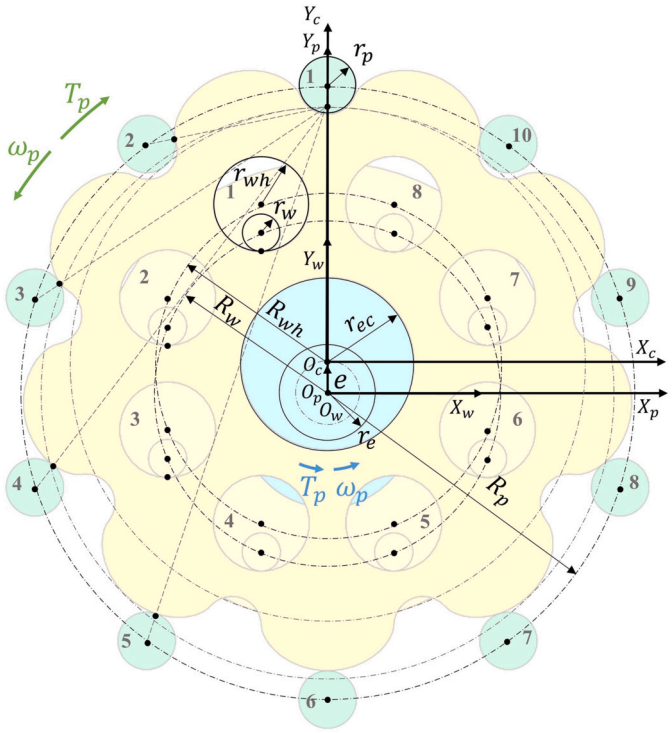


Fig. 3. The coordinate system of the cycloidal drive.

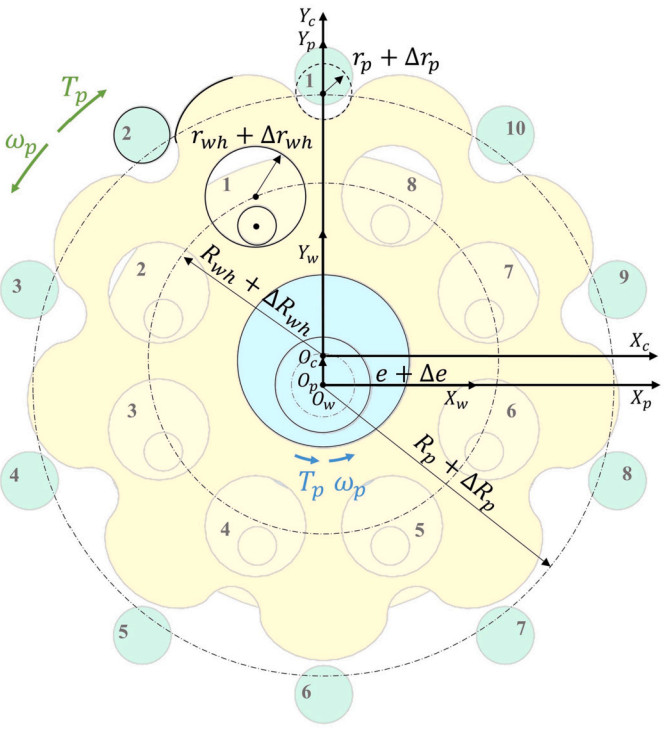


Fig. 5. The geometric parameters with deviations in a cycloidal drive.

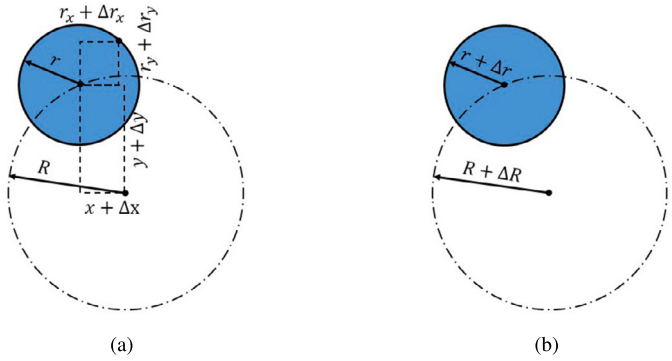


Fig. 4. (a) Actual deviations case, and (b) simplified deviations case in this article.

ponents has relative deviations. However, only the geometric deviations of one component in each pair are necessary for analysis. In this study, we will consider the eccentric shaft deviation Δe, the radius and distribution radius deviations of the pin-hole Δr_{wh} and ΔR_{wh}, and the pin gear geometric deviations Δr_p and ΔR_p. In practice, the priority is usually given to active trimming of the cycloidal gears. In analyzing the deviations between the cycloidal gear and the pin gear, Δr_p and ΔR_p will be applied to the parameters of the cycloidal gear instead of the actual pin gear. Fig. 5 shows the geometric parameters of the cycloidal drive with deviations.

It is important to note that the output pin is not necessarily uniformly distributed. The method proposed in this study is versatile and applicable to scenarios involving non-uniform pin distributions.

In practice, the deviations of a pin on the plane include positional deviations in two directions on the plane and the positional deviation of a point on the contour (circularity), as shown in Fig. 4(a). In order to conveniently describe its positional deviations and unify the simulation of different parameters, we simplify the deviations into distribution radius deviation and radius deviation, as shown in Fig. 4(b). It should be noted that the CDFM is not limited to simplified deviation; its input is the coordinates of points on the pin, and more complex deviations can also be implemented by superimposing deviations in the coordinates of points.

Suppose a more detailed deviation model is desired, we suggest that, during the application of the CDFM, the deviation pattern be altered to random deviations within a specified range, which are then superimposed onto point coordinates and incorporated into the calculations.

Assuming the state shown in Fig. 3 is the initial state, we define the eccentric shaft, cycloidal gear, and pin gear rotation angles as θ_e, θ_c, and θ_p, respectively. In this study, we define the counter-clockwise direction as positive and use “mm” as the unit of displacement and dimension, “N” as the unit of force, “MPa” as the unit of stress, and “Nmm” as the unit of torque in calculations. For display purposes, the torque unit in the charts is “Nm”.

In Fig. 3, we establish a coordinate system for a cycloidal drive, where the output disk coordinate system $\boldsymbol{S}_w\{O_w, X_w, Y_w\}$ is a fixed absolute coordinate system. In order to facilitate the calculation of relevant collision relationships, it is necessary to transform the points under the cycloidal gear coordinate system $\boldsymbol{S}_c\{O_c, X_c, Y_c\}$ and the pin gear coordinate system $\boldsymbol{S}_p\{O_p, X_p, Y_p\}$ into the $\boldsymbol{S}_w$.

The displacement matrix for the transformation from $\boldsymbol{S}_c$ to $\boldsymbol{S}_w$ is given by

$$\mathbf{R}_c^w = \begin{bmatrix} \cos\theta_c & -\sin\theta_c \\ \sin\theta_c & \cos\theta_c \end{bmatrix}, \mathbf{P}_c^w = \begin{bmatrix} -(e+\Delta e)\sin\theta_e \\ (e+\Delta e)\cos\theta_e \end{bmatrix}. \tag{4}$$

The origin of $\boldsymbol{S}_p$ coincides with $\boldsymbol{S}_w$, and the rotation matrix of the transformation from $\boldsymbol{S}_p$ to $\boldsymbol{S}_w$ is given by

$$\mathbf{R}_p^w = \begin{bmatrix} \cos\theta_p & -\sin\theta_p \\ \sin\theta_p & \cos\theta_p \end{bmatrix}. \tag{5}$$

2.1. In the cycloidal gear coordinate system

The coordinates of a point on the curve of the cycloidal gear are given by:

$$\begin{bmatrix} x_c^c \\ y_c^c \end{bmatrix} = \begin{bmatrix} (R_p + \Delta R_p)\sin\varphi_c - e\sin z_p\varphi_c \\ \quad + \dfrac{\left[K_1 \sin z_p\varphi_c - \sin\varphi_c\right](r_p + \Delta r_p)}{\sqrt{1 + K_1^2 - 2K_1\cos z_c\varphi_c}} \\ (R_p + \Delta R_p)\cos\varphi_c - e\cos z_p\varphi_c \\ \quad + \dfrac{\left[K_1 \cos z_p\varphi_c - \cos\varphi_c\right](r_p + \Delta r_p)}{\sqrt{1 + K_1^2 - 2K_1\cos z_c\varphi_c}} \end{bmatrix}, \tag{6}$$

where the curtate coefficient K_1 is denoted by

$$K_1 = \frac{ez_p}{R_p + \Delta R_p}. \tag{7}$$

The normal direction at a point on the curve of the cycloidal gear is given by:

$$\begin{bmatrix} x_{cn}^c \\ y_{cn}^c \end{bmatrix} = \begin{bmatrix} \dfrac{x_c^c - z_c esinz_p\varphi_c}{\sqrt{[x_c^c - z_c esinz_p\varphi_c]^2 + [y_c^c - z_c ecosz_p\varphi_c]^2}} \\ \dfrac{y_c^c - z_c ecosz_p\varphi_c}{\sqrt{[x_c^c - z_c esinz_p\varphi_c]^2 + [y_c^c - z_c ecosz_p\varphi_c]^2}} \end{bmatrix}. \tag{8}$$

The radius of curvature at a point on the curve of the cycloidal gear is given by:

$$\rho_c = \frac{[1 + K_1^2 - 2K_1 cosz_c\varphi_c]^{1.5}}{K_1(1 + z_p)cosz_c\varphi_c - z_p K_1^2 - 1}(R_p + \Delta R_p) + (r_p + \Delta r_p). \tag{9}$$

The radius of curvature value calculated in Equation (9) is negative for convex surfaces and positive for concave surfaces.

Define the output pin identifiers in a counter-clockwise direction ($i_w = 1, 2, ..., z_w$), and the coordinates of a point on the output pin-hole i_w are given by:

$$\begin{bmatrix} x_{wh,iw}^c \\ y_{wh,iw}^c \end{bmatrix} = \begin{bmatrix} -(r_{wh} + \Delta r_{wh})sin\varphi_{wh,iw} \\ \quad -(R_{wh} + \Delta R_{wh})sin\dfrac{(2i_{wh} + 1)\pi}{z_w} \\ (r_{wh} + \Delta r_{wh})cos\varphi_{wh,iw} \\ \quad +(R_{wh} + \Delta R_{wh})cos\dfrac{(2i_{wh} + 1)\pi}{z_w} \end{bmatrix}, \tag{10}$$

where $\varphi_{wh,iw}$ is the counter-clockwise angle between the y-axis and the line connecting the point and the center of the output pin-hole i_w.

The normal direction at a point on the pin-hole i_w is given by:

$$\begin{bmatrix} x_{whn,iw}^c \\ y_{whn,iw}^c \end{bmatrix} = \begin{bmatrix} -sin\varphi_{wh,iw} \\ cos\varphi_{wh,iw} \end{bmatrix}. \tag{11}$$

2.2. In the pin gear coordinate system

Define the roller pin identifiers in a counter-clockwise direction ($i_p = 1, 2, ..., z_p$), and the coordinates of a point on the roller pin i_p are given by

$$\begin{bmatrix} x_{p,ip}^p \\ y_{p,ip}^p \end{bmatrix} = \begin{bmatrix} -(r_p + \Delta r_p)sin(\varphi_{p,ip}) - (R_p + \Delta R_p)sin\dfrac{2\pi(i_p - 1)}{z_p} \\ (r_p + \Delta r_p)cos(\varphi_{p,ip}) + (R_p + \Delta R_p)cos\dfrac{2\pi(i_p - 1)}{z_p} \end{bmatrix}, \tag{12}$$

where $\varphi_{p,ip}$ is the counter-clockwise angle between the y-axis and the line connecting the point and the center of the roller pin i_p.

The normal direction at the roller pin i_p is given by:

$$\begin{bmatrix} x_{pn,ip}^p \\ y_{pn,ip}^p \end{bmatrix} = \begin{bmatrix} -sin\varphi_{p,ip} \\ cos\varphi_{p,ip} \end{bmatrix} \tag{13}$$

2.3. In the output disk coordinate system

The coordinates of a point on the pin i_w are given by:

$$\begin{bmatrix} x_{w,iw}^w \\ y_{w,iw}^w \end{bmatrix} = \begin{bmatrix} -r_w sin(\varphi_{w,iw}) - R_w sin\dfrac{(2i_w + 1)\pi}{z_w} \\ r_w cos(\varphi_{w,iw}) + R_w cos\dfrac{(2i_w + 1)\pi}{z_w} \end{bmatrix}, \tag{14}$$

where $\varphi_{w,iw}$ is the counter-clockwise angle between the y-axis and the line connecting the point and the center of the output pin i_w.

The normal direction at a point on the output pin-hole i_w is given by:

$$\begin{bmatrix} x_{wn,iw}^w \\ y_{wn,iw}^w \end{bmatrix} = \begin{bmatrix} -sin\varphi_{w,iw} \\ cos\varphi_{w,iw} \end{bmatrix}. \tag{15}$$

The coordinates of a point on the cycloidal gear can be transformed from $\boldsymbol{S}_c$ to $\boldsymbol{S}_w$ by the following equation:

$$\begin{bmatrix} x_c^w \\ y_c^w \end{bmatrix} = \mathbf{R}_c^w \begin{bmatrix} x_c^c \\ y_c^c \end{bmatrix} + \mathbf{P}_c^w. \tag{16}$$

The normal direction at a point on the cycloidal gear can be transformed from $\boldsymbol{S}_c$ to $\boldsymbol{S}_w$ by the following equation:

$$\begin{bmatrix} x_{cn}^w \\ y_{cn}^w \end{bmatrix} = \mathbf{R}_c^w \begin{bmatrix} x_{cn}^c \\ y_{cn}^c \end{bmatrix} + \mathbf{P}_c^w. \tag{17}$$

The coordinates of a point on the output pin-hole i_w can be transformed from $\boldsymbol{S}_c$ to $\boldsymbol{S}_w$ by the following equation:

$$\begin{bmatrix} x_{wh,iw}^w \\ y_{wh,iw}^w \end{bmatrix} = \mathbf{R}_c^w \begin{bmatrix} x_{wh}^c \\ y_{wh}^c \end{bmatrix} + \mathbf{P}_c^w. \tag{18}$$

The normal direction at a point on the output pin-hole i_w can be transformed from $\boldsymbol{S}_c$ to $\boldsymbol{S}_w$ by the following equation:

$$\begin{bmatrix} x_{whn,iw}^w \\ y_{whn,iw}^w \end{bmatrix} = \mathbf{R}_c^w \begin{bmatrix} x_{whn,iw}^c \\ y_{whn,iw}^c \end{bmatrix} + \mathbf{P}_c^w. \tag{19}$$

The coordinates of a point on the roller pin i_p can be transformed from $\boldsymbol{S}_p$ to $\boldsymbol{S}_w$ by the following equation:

$$\begin{bmatrix} x_{p,ip}^w \\ y_{p,ip}^w \end{bmatrix} = \mathbf{R}_p^w \begin{bmatrix} x_{p,ip}^p \\ y_{p,ip}^p \end{bmatrix}. \tag{20}$$

The normal direction at a point on the roller pin i_p can be transformed from $\boldsymbol{S}_p$ to $\boldsymbol{S}_w$ by the following equation:

$$\begin{bmatrix} x_{pn,ip}^w \\ y_{pn,ip}^w \end{bmatrix} = \mathbf{R}_p^w \begin{bmatrix} x_{pn,ip}^p \\ y_{pn,ip}^p \end{bmatrix}. \tag{21}$$

All subsequent analyses and calculations are conducted in the coordinate system $\boldsymbol{S}_w$. This study focuses on one cycloidal gear as the object of analysis and assumes that, in practice, forces on two or more cycloidal gears are evenly spaced. The number of cycloidal gears is denoted by n_c.

3. Numerical analysis method CDFM for cycloidal drives

The analysis of cycloidal drives revolves around the contact analysis of three pairs of interacting components:

1. the eccentric shaft (E) and the cycloidal gear (C);
2. the output pin-holes (WH) and the output pins (W);
3. the roller pins (P) on the pin gear and the cycloidal gear (C).

This study proposes a numerical model analysis method to address clearance, deformation, and friction issues in contact analysis. In each contact analysis pair, the model first considers the unloaded contact, as

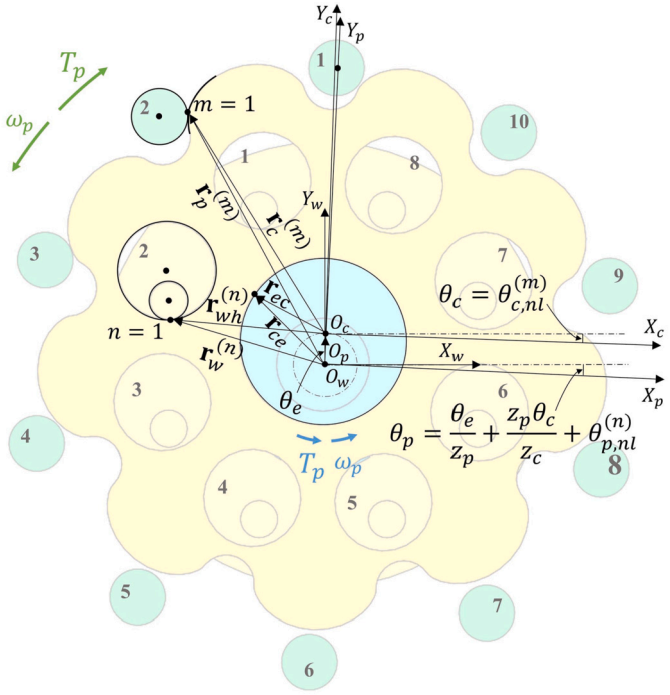


Fig. 6. Diagram of the cycloidal drive without load.

illustrated in Fig. 6, to calculate the component deflection caused by the possible contact points. Based on the unloaded analysis, the model uses deformation constraints to establish a load analysis based on contact force and contact torque conditions, as depicted in Fig. 7. In the contact analysis under load, the deformation of the eccentric shaft adopts a fixed stiffness to simplify shaft stiffness involving multiple deformations, and the deformations of the other components are based on the Hertz contact theory to analyze the non-linear stiffness of each contact point in detail [19,33]. The model also calculates the corresponding friction force and friction torque through the contact force. Through the above analysis, the model establishes the functional relationship between the contact force, contact torque, friction force, and friction torque in each contact analysis pair. The force balance and torque balance relationships of individual components are then used to establish constraint conditions. Finally, by solving the nonlinear equation system, the model obtains the contact force and contact torque that satisfies the external load and then solves for all contact components. The proposed clearance, deformation, and friction numerical analysis method (CDFM) for cycloidal drives is illustrated in Fig. 8.

3.1. Hertzian contact theory

The CDFM uses Hertzian contact theory to analyze the deformation during contact [19,33]. According to Hertzian contact theory, when the contact curvature radius is ρ_1 and ρ_2, the contact surface thickness is b, the contact force is F_c, two objects with Young's modulus of E_1 and E_2 and Poisson's ratio of ν_1 and ν_2 have the following deformation relations at the contact location:

$$\begin{cases} a &= \sqrt{\dfrac{4F_c\rho^*\left[E_1\left(1-\upsilon_1^2\right)+E_2\left(1-\upsilon_2^2\right)\right]}{\pi b E_1 E_2}} \\ \delta &= \dfrac{2F_c}{\pi b}\left[\dfrac{1-\nu_1^2}{E_1}\left(\ln\dfrac{4|\rho_1|}{a}-\dfrac{1}{2}\right)+\dfrac{1-\nu_2^2}{E_2}\left(\ln\dfrac{4|\rho_2|}{a}-\dfrac{1}{2}\right)\right] \\ \sigma &= \dfrac{2F_c}{\pi ab} \end{cases}, \tag{22}$$

where a is half the contact deformation width, δ is the deformation, σ is the contact stress, and ρ^* is the equivalent contact radius. Two cases exist:

In the "Convex and Convex" case, as in Fig. 9(a):

$$\rho^* = \left|\frac{\rho_1\rho_2}{\rho_1+\rho_2}\right|; \tag{23}$$

In the "Convex and Concave" case, as in Fig. 9(b).

$$\rho^* = \left|\frac{\rho_1\rho_2}{\rho_1-\rho_2}\right|. \tag{24}$$

In the CDFM, the contact between the output pins and the output pin-holes is consistent with the "Convex and Concave" case. Since the "Convex" curvature is negative, and the "Concave" curvature is positive in the Equation (9), the contact calculation between the pin gear and the cycloidal gear is also calculated using the "Convex and Concave" case.

Define contact parameters of the cycloidal gear, pin gear, output pins, and pin-holes: E_c, E_p, E_w and E_{wh} for Young's modulus; ν_c, ν_p, ν_w and ν_{wh} for Poisson's ratio. The thickness of the contact surface between the output pins and pin-holes is b_w, and their curvature radiuses are $(r_{wh}+\Delta r_{wh})$ and r_w separately. The thickness of the pin gear between the cycloidal gear is b_p, and their curvature radiuses are r_p and ρ_c separately.

Through Equation (22) and Equation (24), the contact deformation δ can be solved by F_c. Similarly, the inverse of Equation (22) and Equation (24) can be solved for the contact force F_c by δ. The equation is a complex nonlinear function, so its inverse operation relies on the numerical solution.

3.2. Contact analysis of the eccentric shaft E and the cycloidal gear C

The cycloidal gear is generally connected to the eccentric shaft through a roller bearing, and a contact force $\mathbf{F}_{ec,c}$ exists between the two, with the direction along the normal direction of the equivalent contact point. Consider the dynamic friction and damping coefficients at this bearing as μ_{ec} and c_{ec}, respectively. The frictional force $\mathbf{F}_{ec,f}$ transmitted from the eccentric shaft to the cycloidal through the bearing, reversing along the direction tangential to the equivalent contact point, can be obtained with the magnitude:

$$F_{ec,f} = \mu_{ec}F_{ec,c} + c_{ec}\upsilon_{ec}, \tag{25}$$

where υ_e is the magnitude of the relative sliding velocity at the equivalent contact point.

In turn, the frictional torque of the cycloidal gear from the eccentric shaft is obtained by:

$$\mathbf{T}_{ec,f} = \mathbf{F}_{ec,f}\mathbf{r}_{ec}, \tag{26}$$

where $\mathbf{r}_{ec}$ is the position vector at the contact point between the eccentric shaft and the cycloidal gear relative to the center of the cycloidal gear.

The combined force on the eccentric shaft from the cycloidal gear is

$$\mathbf{F}_{ce} = -(\mathbf{F}_{ec,c} + \mathbf{F}_{ec,f}). \tag{27}$$

$\mathbf{F}_{ce}$ will cause the eccentric shaft to deform, which in turn leads to the offset of the center position of the cycloidal gear. The deformation of the eccentric shaft and the cycloidal gear is complex. It contains the deformation of the bearings on the eccentric shaft and the combined deformation caused by the deformation of the eccentric shaft itself. The stiffness of this deformation process is defined as K_e.

The offset of the center of the cycloidal can be obtained as

$$\boldsymbol{\delta}_{cw} = \frac{\mathbf{F}_{ce}}{K_e} \tag{28}$$

Considering the above offsets, the transformation matrix $\mathbf{P}_c^w$ needs to add additional offsets to become $\mathbf{P}_c^w + \boldsymbol{\delta}_{cw}$.

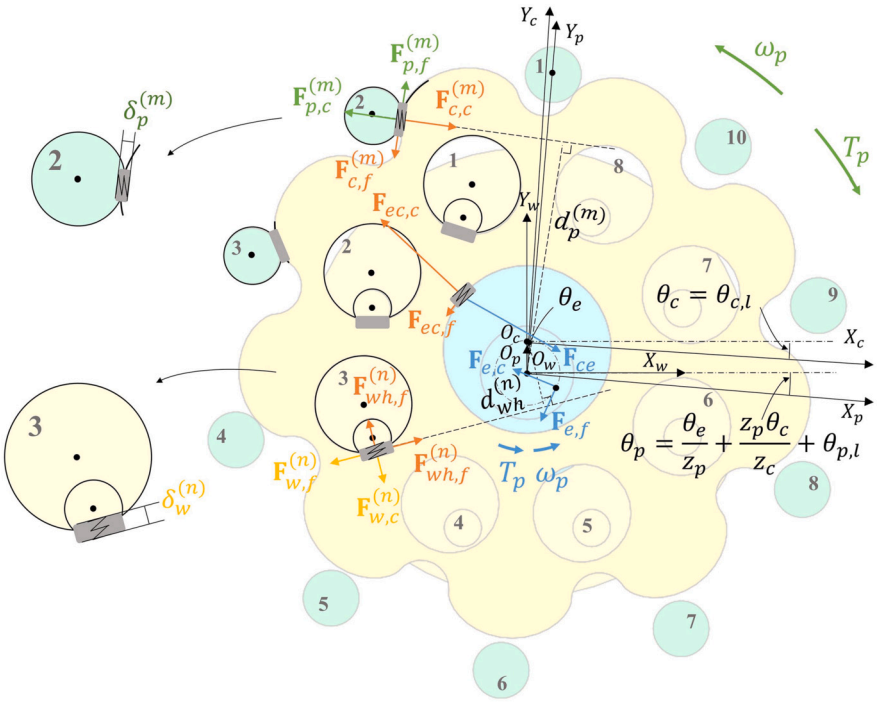


Fig. 7. Diagram of the cycloidal drive with load.

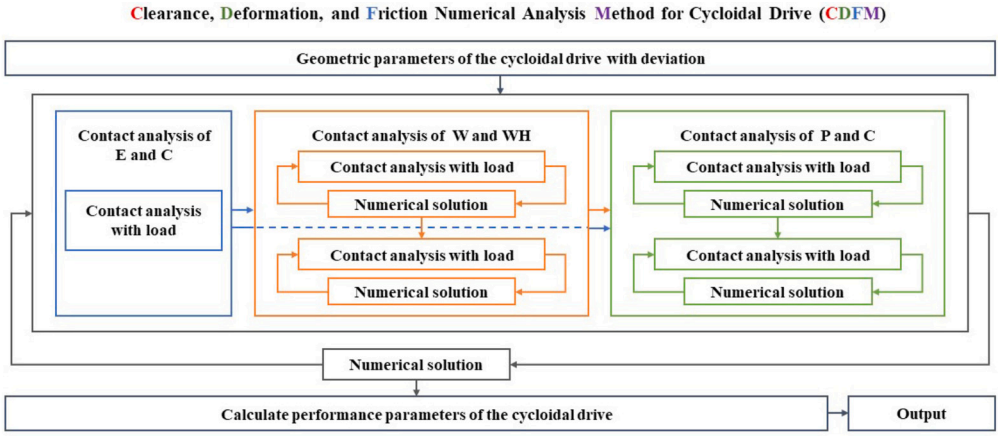


Fig. 8. Diagram of the numerical analysis method CDFM for cycloidal drives.

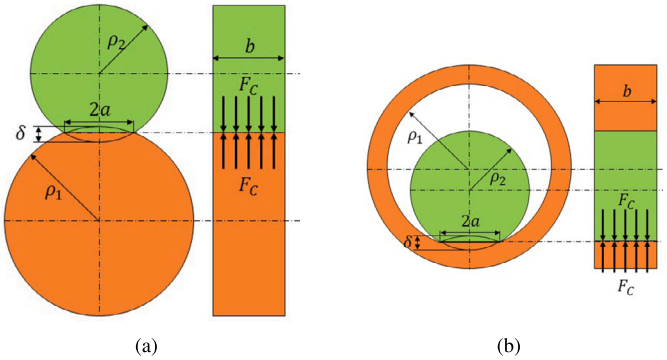


Fig. 9. (a) "Convex and Convex" case, and (b) "Convex and Concave" case.

3.3. Contact analysis of the output pins W and pin-holes WH

3.3.1. No-load contact analysis

Before analyzing the load contact of output pins and pin-holes, it is necessary to analyze the no-load contact condition. The purpose is to identify the output pins and pin-holes that may have contact forces under clearances condition and the additional rotation angle of cycloidal gear to meet the contact condition. The analysis process is as follows:

Step 1. Identify the output pins and pin-holes that may have contact force.
The output pins and pin-holes that may have contact force are judged according to the direction of the torque load under the ideal no-clearances condition and denoted as $i_{w,nl}$, where $i_{w,nl} = 1, 2, ..., z_{w,nl}$.

Step 2. Calculate the rotation angle of the cycloidal gear when the output pin $i_{w,nl}$ is just in contact under the clearance condition.
In the ideal no-clearances condition, the rotation angle of the cycloidal gear is defined as $\theta_{c,nc} = 0$. In the clearance condition, when the actual rotation angle of cycloidal gear $\theta_c = \theta_{c,nc}$, the output pins do not contact the output pin-holes. In order to make the output pin and the output pin-hole just contact, the cycloidal gear needs to rotate an additional angle $\theta_{c,nl}$, and the rotation angle of the cycloidal gear is $\theta_c = \theta_{c,nc} + \theta_{c,nl} = \theta_{c,nl}$.

When the output pin and pin-hole $i_{w,nl}$ are just in contact, the coordinate of the output pin contact point is equal to the coordinate of the output pin-hole contact point, and the normal direction at the output pin contact point is opposite to the normal direction at the output pin-hole contact point, namely, the following equation is satisfied.

$$\begin{cases} x^w_{wh,iw} = x^w_{w,iw} \\ y^w_{wh,iw} = y^w_{w,iw} \\ x^w_{whn,iw} y^w_{wn,iw} = -x^w_{wn,iw} y^w_{whn,iw} \end{cases} \tag{29}$$

Solving the nonlinear system Equation (29) to get the parameters $\varphi_{w,iw}$, $\varphi_{wh,iw}$, and $\theta_{c,nl}$, denoted by $\varphi_{w,iwnl}$, $\varphi_{wh,iwnl}$ and $\theta_{c,iwnl}$, respectively. They are the related parameters when the output pin and pin-hole $i_{w,nl}$ are just in contact.

Step 3. Sort the output pins and pin-holes that may have contact forces.
Taking the ascending order of $|\theta_{c,iwnl}|$ as a reference, the above output pins and the pin-holes $i_{w,nl}$ are sorted to $i^{(n)}_{w,nl}$, and the corresponding parameters and the angle of the cycloidal gear are $\varphi^{(n)}_{w,nl}$, $\varphi^{(n)}_{wh,nl}$ and $\theta^{(n)}_{c,nl}$, where $n = 1, 2, ..., z_{w,nl}$. The output pin $i^{(1)}_{w,nl}$ will be the first contact with load.

Step 4. Obtain coordinates of the contact points.
By $\varphi^{(n)}_{w,nl}$, $\varphi^{(n)}_{wh,nl}$, and $\theta^{(n)}_{c,nl}$, the coordinates of the contact point contact can be obtained.

3.3.2. Load contact analysis

Under load, for each contact, the cycloidal gear needs to rotate first the clearance angle and then the contact deformation angle. Define the additional angle of the cycloidal gear under load as $\theta_{c,l}$, and the actual angle of the cycloidal gear $\theta_c = \theta_{c,nc} + \theta_{c,l} = \theta_{c,l}$. In the above output pins and pin-holes that may have contact forces, some are not in contact because their clearances are too large. Define the number of output pins in contact as $z_{w,l}$.

The combined contact torque $\mathbf{T}_{wh,c}$ of the cycloidal gear through output pin-holes is given and satisfies the following equation,

$$\mathbf{T}_{wh,c} = \sum_{n=1}^{z_{w,l}} \mathbf{F}^{(n)}_{wh,c} \times \mathbf{r}^{(n)}_{wh}, \tag{30}$$

where $\mathbf{r}^{(n)}_{wh}$ is the position vector at the contact point relative to the center of the cycloidal gear.

$\mathbf{F}^{(n)}_{wh,c}$ is the contact force, and its magnitude $F^{(n)}_{wh,c}$ is calculated from the contact deformation $\delta^{(n)}_{wh}$ according to the Hertzian contact theory, along the normal direction of the contact point.

The contact deformation $\delta^{(n)}_{wh}$ can be calculated using $\theta_{c,l}$, and $\theta^{(n)}_{c,nl}$ by the following equation,

$$\delta^{(n)}_{wh} = |\theta_{c,l} - \theta^{(n)}_{c,nl}| d^{(n)}_{wh}, \tag{31}$$

where $d^{(n)}_{wh}$ is the distance from the center of the cycloidal gear to the normal of the contact point.

The load contact of output pins and pin-holes can be analyzed by the following process:

Step 1. Identify the output pins and pin-holes that have contact force under load.
Through the previous no-load contact analysis, it is known that the output pins $i^{(n)}_{w,nl}$ that may have contact forces and the absolute value of the deflection angle $|\theta^{(n)}_{c,nl}|$ corresponding to the output pins $i^{(n)}_{w,nl}$ increases sequentially from $n = 1$ to $n = z_{w,nl}$.
Taking $n = 1$ to $n = z_{w,nl}$ in turn, the $\mathbf{T}^{(n)}_{wh,c}$ is calculated according to the corresponding condition that $\theta_{c,l} = \theta^{(n)}_{c,nl}$ until $T^{(n)}_{wh,c} > T_{wh,c}$ is satisfied for the first time, and the number of output pins that have contact forces can be obtained as $z_{w,l} = n - 1$. If $n = z_{w,nl}$, it still does not satisfy $T^{(n)}_{wh,c} > T_{wh,c}$, then we can get $z_{w,l} = n$.

Step 2. Calculate contact force and contact torque.
Using $z_{w,l}$ and $\mathbf{T}_{wh,c}$, the nonlinear implicit system of equations consisting of Equation (22), Equation (30) and Equation (31) can be solved numerically to calculate the deflection angle of the cycloidal gear with load $\theta_{c,nl}$.
Further, according to Equation (22) and Equation (31), the contact force $\mathbf{F}^{(n)}_{wh,c}$ for each output pin-hole in contact can be obtained, where $n = 1, 2, ..., z_{w,nl}$, and the combined torque $\mathbf{F}_{wh,c}$ of cycloidal gear through output pin-holes can also be obtained.
Similarly, the combined contact force $\mathbf{F}_{w,c}$ of the output disk through output pins and the combined contact torque $\mathbf{T}_{w,c}$ can also be obtained.

Step 3. Calculate contact friction and contact friction torque.
Define the coefficients of dynamic friction and damping of the contact between the output pins and the pin-holes as μ_w and c_w, respectively. The friction force $\mathbf{F}^{(n)}_{wh,f}$ of the output pin-hole in contact is along the tangential direction of the contact point and has the magnitude:

$$F^{(n)}_{wh,f} = \mu_w F^{(n)}_{wh,c} + c_w v^{(n)}_w, \tag{32}$$

where $v^{(n)}_w$ is the magnitude of the relative sliding velocity at the contact point.
Further, the combined friction force $\mathbf{F}_{wh,f}$ and the combined friction torque $\mathbf{T}_{wh,f}$ of the cycloidal gear through output pin-holes can be obtained.

3.4. Contact analysis of the pin gear P and the cycloidal gear C

3.4.1. No-load contact analysis

Similarly, it is necessary to analyze the no-load contact condition before analyzing the load contact of the pin gear and the cycloidal gear. The purpose is to identify the roller pins that may have contact forces under the clearance condition and the additional rotation angle of the pin gear to meet the contact condition. The analysis process is as follows:

Step 1. Identify the roller pins that may have contact forces.
The roller pins that may have contact force are judged according to the direction of the torque load under the ideal no-clearance condition and denoted as $i_{p,nl}$, where $i_{p,nl} = 1, 2, ..., z_{p,nl}$.

Step 2. Calculate the rotation angle of the pin gear when the roller pin $i_{p,nl}$ is just in contact under the clearance condition.
In the ideal no-clearance condition, the rotation angle of the pin gear is defined as $\theta_{p,nc} = \theta_e / z_p + z_c \theta_c / z_p$. In the clearance condition, when the actual rotation angle of pin gear $\theta_p = \theta_{p,nc}$, the roller pins do not contact the cycloidal gear. In order to make the roller pins and the cycloidal gear just contact, the pin gear needs to rotate an additional angle $\theta_{p,nl}$, and the rotation angle of the cycloidal gear is $\theta_p = \theta_{p,nc} + \theta_{p,nl}$.
When the roller pin $i_{p,nl}$ is just in contact, the coordinate of the roller pin contact point is equal to the coordinate of the cycloidal gear contact point. The normal direction at the roller pin contact point is opposite to that at the cycloidal gear contact point. Namely, the following equation is satisfied.

$$\begin{cases} x^w_{p,ip} = x^w_c \\ y^w_{p,ip} = y^w_c \\ x^w_{pn,ip} y^w_{cn} = -y^w_{pn,ip} x^w_{cn} \end{cases} \tag{33}$$

Solving the nonlinear system Equation (33) to get the parameters $\varphi_{p,ip}$, φ_c, and $\theta_{p,nl}$, denoted by $\varphi_{p,ipnl}$, $\varphi_{c,ipnl}$, and $\theta_{p,ipnl}$,

respectively. They are the related parameters when the roller pin $i_{p,nl}$ is just in contact.

Step 3. Sort the roller pins that may have contact forces.
Taking the ascending order of $|\theta_{p,ipnl}|$ as a reference, the above roller pins $i_{p,nl}$ with the pin-hole $i_{p,nl}$ is sorted to $i_{p,nl}^{(m)}$, and the corresponding parameters and the angle of pin gear are $\varphi_{p,nl}^{(m)}$, $\varphi_{c,nl}^{(m)}$, and $\theta_{p,nl}^{(m)}$, where $m = 1, 2, ..., z_{p,nl}$. The roller pin $i_{p,nl}^{(1)}$ will be the first contact with load.

Step 4. Obtain coordinates and curvature radius of the contact points.
By $\varphi_{p,nl}^{(m)}$, $\varphi_{c,nl}^{(m)}$, and $\theta_{p,nl}^{(m)}$, the coordinates and curvature radius of the contact point contact can be obtained.

3.4.2. Load contact analysis

Under load, for each contact, the pin gear needs to rotate first the clearance angle and then the contact deformation angle. Define the additional angle of the pin gear under load as $\theta_{p,l}$, and the actual angle of the pin gear is $\theta_{p,nc} = \theta_e/z_p + z_c\theta_{c,l}/z_p$. For the above roller pins that may have contact forces, some roller pins are not in contact because their clearances of them are too large. Define the number of pins in contact as $z_{p,l}$.

The combined contact torque $\mathbf{T}_{p,c}$ of the pin gear through roller pins are given and satisfies the following equation,

$$\mathbf{T}_{p,c} = \sum_{n=1}^{z_{p,l}} \mathbf{F}_{p,c}^{(m)} \times \mathbf{r}_p^{(m)}, \tag{34}$$

where $\mathbf{r}_p^{(m)}$ is the position vector at the contact point relative to the center of the pin gear.

$\mathbf{F}_{p,c}^{(m)}$ is the contact force, and its magnitude $F_{p,c}^{(m)}$ is calculated from the contact deformation $\delta_p^{(m)}$ according to the Hertzian contact theory, along the normal direction of the contact point.

The contact deformation δ_p^c can be calculated using $\theta_{p,l}$, and $\theta_{p,nl}^{(m)}$ by the following equation,

$$\delta_p^{(m)} = |\theta_{p,l} - \theta_{p,nl}^{(m)}| d_p^{(m)}, \tag{35}$$

where $d_p^{(m)}$ is the distance from the center of the pin gear to the normal of the contact point.

The load contact of the pin gear and the cycloidal gear can be analyzed by the following process:

Step 1. Identify the roller pins that have contact force under load.
Through the previous no-load contact analysis, it is known that the roller pins $i_{p,nl}^{(m)}$ that may have contact forces and the absolute value of the deflection angle $|\theta_{p,nl}^{(m)}|$ corresponding to the roller pins $i_{p,nl}^{(m)}$ increases sequentially from $m = 1$ to $m = z_{p,nl}$.
Taking $m = 1$ to $m = z_{p,nl}$ in turn, the $\mathbf{T}_{p,c}^{(m)}$ is calculated according to the corresponding condition that $\theta_{p,l} = \theta_{p,nl}^{(m)}$ until $T_{p,c}^{(m)} > T_{p,c}$ is satisfied for the first time, and the number of roller pins that have contact forces can be obtained as $z_{p,l} = m - 1$. If $m = z_{p,nl}$, it still does not satisfy $T_{p,c}^{(m)} > T_{p,c}$, then we can get $z_{p,l} = m$.

Step 2. Calculate contact force and contact torque.
Using $z_{p,l}$ and $\mathbf{T}_{p,c}$, the nonlinear implicit system of equations consisting of Equation (22), (34) and (35) can be solved numerically to calculate the deflection angle of the pin gear with load $\theta_{p,nl}$.
Further, according to Equation (22) and (35), the contact force $\mathbf{F}_{p,c}^{(m)}$ for each roller pin in contact can be obtained, where $m = 1, 2, ..., z_{p,nl}$, and the combined torque $\mathbf{F}_{p,c}$ of pin gear can also be obtained. Similarly, the combined contact force $\mathbf{F}_{c,c}$ and the combined contact torque $\mathbf{T}_{c,c}$ of the cycloidal gear can also be obtained.

Step 3. Calculate contact friction and contact friction torque.
Define the coefficients of dynamic friction and damping of the contact between the roller pins and the cycloidal gear as μ_p and c_p. The friction force $\mathbf{F}_{p,f}^{(m)}$ of the output pin-hole in contact is along the tangential direction of the contact point and has the magnitude:

$$F_{p,f}^{(m)} = \mu_p F_{p,c}^{(m)} + c_p v_p^{(m)}, \tag{36}$$

where $v_p^{(m)}$ is the magnitude of the relative sliding velocity at the contact point.
Further, the combined friction force $\mathbf{F}_{p,f}$ and the combined friction torque $\mathbf{T}_{p,f}$ of the cycloidal gear can be obtained. Similarly, the combined friction force $\mathbf{F}_{c,f}$ and the combined friction torque $\mathbf{T}_{c,f}$ of the cycloidal gear can also be obtained.

3.5. Load contact analysis of the whole cycloidal drive

The calculation of friction force is an implicit solution process, which always requires a known contact force to solve the contact friction force. Define the solution process of the sections 3.2, 3.3, and 3.4 as the following functions, respectively.

$$(\mathbf{F}_{ec,f}, \mathbf{T}_{ec,f}, \mathbf{T}_{ec,f}, \boldsymbol{\delta}_{cw}) = f_e(\mathbf{F}_{ec,c}) \tag{37}$$

$$(\mathbf{F}_{wh,c}, \mathbf{F}_{wh,f}, \mathbf{T}_{wh,f}, \theta_{c,l}) = f_w(\mathbf{T}_{wh,c}, \boldsymbol{\delta}_{cw}) \tag{38}$$

$$(\mathbf{F}_{c,c}, \mathbf{F}_{c,f}, \mathbf{T}_{c,c}, \mathbf{T}_{c,f}, \mathbf{T}_{p,f}) = f_p(\mathbf{T}_{p,c}, \theta_{c,l}, \boldsymbol{\delta}_{cw}) \tag{39}$$

Define the external torque on the pin gear as $\mathbf{T}_p = \mathbf{T}_{out}/n_c$. Establish the constraints based on the pin gear torque balance, cycloidal gear torque balance, and force balance as follows.

$$\mathbf{T}_{p,c} + \mathbf{T}_{p,f} + \mathbf{T}_p = 0 \tag{40}$$

$$\mathbf{T}_{c,c} + \mathbf{T}_{c,f} + \mathbf{T}_{wh,c} + \mathbf{T}_{wh,f} + \mathbf{T}_{ec,c} + \mathbf{T}_{ec,f} = 0 \tag{41}$$

$$\mathbf{F}_{c,c} + \mathbf{F}_{c,f} + \mathbf{F}_{wh,c} + \mathbf{F}_{wh,f} + \mathbf{F}_{ec,c} + \mathbf{F}_{ec,f} = 0 \tag{42}$$

Solving the above system of nonlinear equations, we can obtain $\mathbf{T}_p$, $\mathbf{T}_{wh,c}$ and $\mathbf{T}_{p,c}$, and $\mathbf{F}_{ec,c}$, and then we can solve for all the loaded contact parameters on the cycloidal gear, pin gear, output pins, and output pin-holes, including the coordinates of contact points, contact forces, and contact friction.

The contact torque of the combined force ($\mathbf{F}_{ce}$) on the eccentric shaft from the cycloidal gear, denoted by $\mathbf{T}_{e,c}$, is as follows:

$$\mathbf{T}_{e,c} = \mathbf{F}_{ce} \times \mathbf{r}_{ce} = -(\mathbf{F}_{ec,c} + \mathbf{F}_{ec,f}) \times \mathbf{r}_{ce}, \tag{43}$$

where $\mathbf{r}_{ce}$ is the position vector relative to the eccentric shaft center at the contact point between the eccentric shaft and the cycloidal gear.

The external input torque to the input shaft is

$$\mathbf{T}_e = -\mathbf{T}_{e,c} - \mathbf{T}_{e,f}. \tag{44}$$

$\mathbf{T}_{e,f}$ is the friction torque on the input shaft from the dynamic friction force and the damping force.

$$F_{e,f} = \mu_e F_{e,c} + c_e r_e \omega_e \tag{45}$$

$$T_{e,f} = T_{e,f} r_e \tag{46}$$

μ_e and c_e are the coefficients of dynamic friction and damping of the input shaft, respectively. The magnitude of the radial force on the input shaft from the cycloidal gear can be solved through

$$F_{e,c} = L_2 F_{ce}/L_1, \tag{47}$$

based on the deflection torque balance of the eccentric input shaft, as shown in Fig. 10.

It should be noted that the above input and output torques are calculated and analyzed according to the case of a single cycloidal gear.

Table 1
Experimental parameters with different geometric deviations.

Parameters	Values		
	Case A	Case B	Case C
Eccentric distance deviation Δe (mm)	0	0.005	**−0.005**
Roller pin radius deviation Δr_p (mm)	0	0.01	0.01
Roller pin distribution deviation ΔR_p (mm)	0	−0.01	−0.01
Output pin-hole radius deviation Δr_{wh} (mm)	0	0.01	0.01
Output pin-hole distribution deviation ΔR_{wh} (mm)	0	0.003	0.003
Ideal eccentric distance e (mm)	0.8	0.8	0.8
Ideal roller pin radius r_p (mm)	1.5	1.5	1.5
Teeth number of pin gear z_p	30		
Eccentric shaft stiffness K_e (N/mm)	-	5×10^6	5×10^6
Ideal roller pin distribution radius R_p (mm)	30		
Number of cycloidal gear n_c	2		
Number of output pin-holes z_w	8		
Ideal output pin radius r_w (mm)	3.5		
Ideal output pin distribution radius R_w (mm)	21		
Ideal output pin-hole radius r_{wh} (mm)	4.3		
Ideal output pin-hole distribution radius R_{wh} (mm)	21		
Radius of eccentric shaft r_{ec} (mm)	15		
Radius of input shaft r_e (mm)	8		
Contact width b_w, and b_p (mm)	6		
Young modulus E_c, E_p, E_{wh} and E_w (MPa)	2×10^5		
Poisson's ratio ν_c, ν_p, ν_{wh} and ν_w	0.3		
Eccentric shaft length parameter L_1	18		
Eccentric shaft length parameter L_2	10		
Friction coefficient μ_e and μ_{ec}	0.01		
Friction coefficient μ_c and μ_p	0.002		
Damping coefficient c_e and c_{ec} (N s/mm)	0.001		
Damping coefficient c_c and c_p (N s/mm)	0.002		

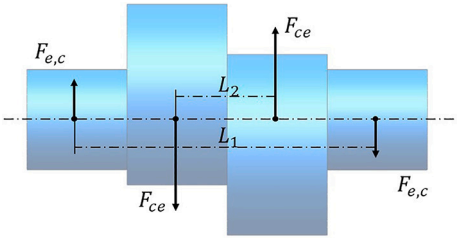


Fig. 10. Diagram of the forces on the eccentric input shaft.

For the case of multiple cycloidal gears, the relevant load parameters are uniformly distributed according to the number of cycloidal gears n_c in the CDFM, and the input torque $\mathbf{T}_{in} = n_c\mathbf{T}_e$.

During the transmission process, there are fluctuations in the transmission ratio of the cycloidal gear due to the presence of clearance. The overall motion is translated into the rotational coordinate system in the eccentric shaft, where the transmission ratio from the pin gear to the cycloidal gear is defined as I_{pc}, and the transmission ratio from the pin-hole to the output pin is I_{whw}. Through the conservation of non-frictional power in transmission, the contact torque can be used to calculate I_{pc} and I_{whw}, and the overall actual transmission ratio $I_{ep,a}$ is as follows:

$$I_{pc} = \frac{T_{c,c}}{T_{p,c}}, I_{whw} = \frac{T_{w,c}}{T_{wh,c}}, I_{ep,a} = \frac{1}{1 - I_{pc}I_{whw}}. \tag{48}$$

Further, calculate the instantaneous average efficiency:

$$\eta_{ep} = \frac{T_{out}}{I_{ep,a}T_{in}} \tag{49}$$

4. Simulation experiments and discussion

To demonstrate and test the application of the CDFM, we set up experiments to analyze the performance of a cycloidal drive with different parameters and focus on the effects of geometric deviations, teeth numbers, and friction coefficients on the cycloidal drive.

4.1. Effects of geometric deviations on cycloidal drive

First, we set up three sets of different geometric deviations shown in Table 1 to show the effects of geometric deviations. Among them, case A is an ideal cycloidal drive model without clearance and ignores the influence of eccentric shaft stiffness as an ideal theoretical reference model; case B uses the same basic design parameters based on case A but considers the clearances, where the eccentricity deviation of the eccentric shaft is positive; case C adjusts the eccentricity deviation of the eccentric shaft to negative based on case B. The above models with clearance deviations all adopt the same deviation size, and there is only a difference in direction, equivalent to assuming the same tolerance value.

Under the conditions of clockwise load torque $T_{out} = 60$ Nm (6×10^4 Nmm), counterclockwise input speed $\omega_e = 200$ rad/s, and eccentric shaft angle $\theta_e = 0$ rad, the force states of the cycloidal gears were simulated for the three sets of geometric parameters. The force states of the cycloidal gears are shown in Fig. 11, where the size of the forces is proportional to the length of the corresponding lines, but the lines representing friction forces F_f are enlarged 30 times than contact forces F_c for clarity.

4.1.1. The load capacity of the cycloidal drives in case A, B, and C

The load capacity of cycloidal drives can be evaluated regarding contact forces and stresses. The lower the contact stress at the same load, the better the load capacity. Fig. 12 shows the contact forces and stresses on the roller pins for the condition of clockwise loading torque $T_{out} = 60$ Nm, input counterclockwise speed $\omega_e = 200$ rad/s, and eccentric shaft angle $\theta_e = 0$ rad. Fig. 13 shows the forces and contact stresses of the output pins under the above conditions. Only the roller pins in contact and output pins in contact are shown. Fig. 14(a) shows the contact force between the cycloidal and the eccentric shaft in the above condition, where $\theta_e \in [0, 2\pi]$.

In Fig. 12(a), it can be seen that in the ideal case A with no clearances, the meshing force on the rollers is significantly lower than in other non-ideal cases with clearances since almost half of the rollers are engaged. Case C, which uses a negative eccentric shaft deviation, has

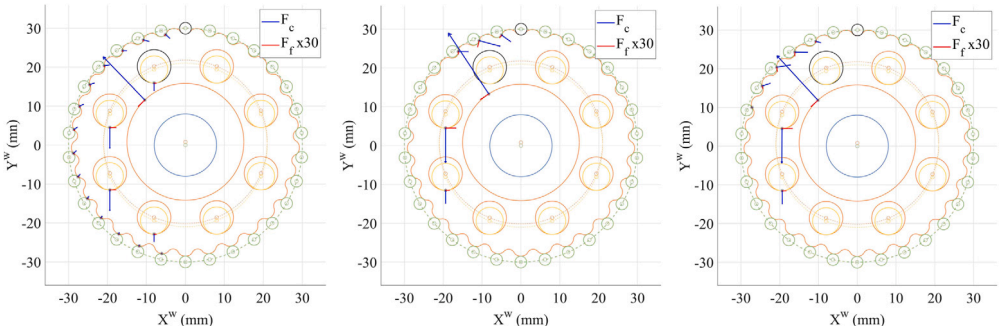


Fig. 11. Force state of the cycloidal gear in (a) case A, (b) case B, and (c) case C.

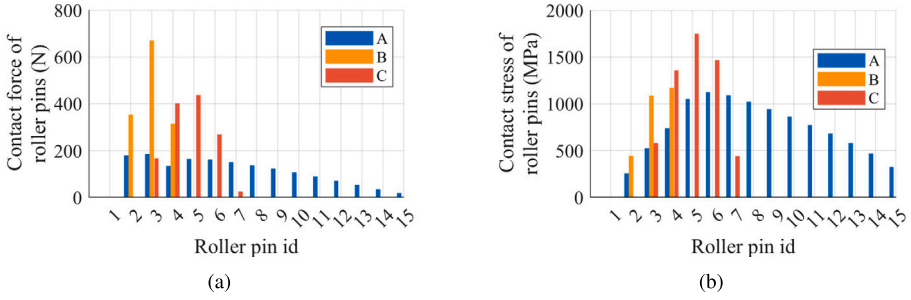


Fig. 12. (a) The contact forces of the roller pins, and (b) The contact stresses of the roller pins in case A, B, and C.

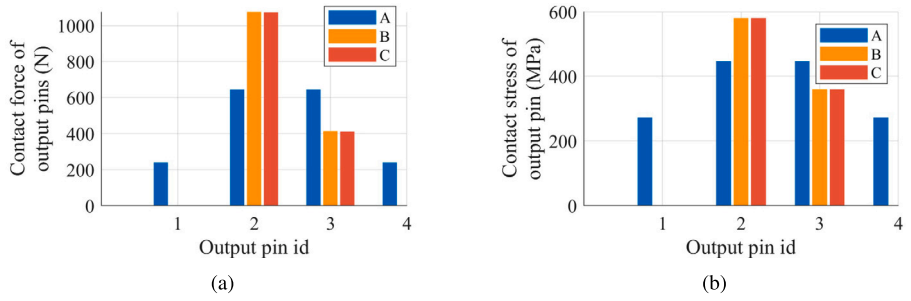


Fig. 13. (a) The contact forces of the output pins, and (b) the contact stresses of the output pins in case A, B, and C.

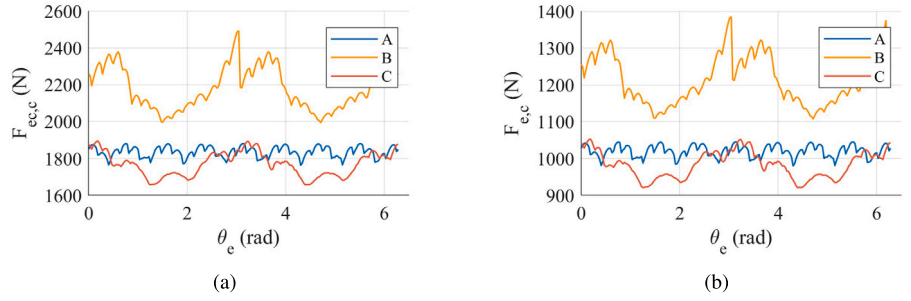


Fig. 14. (a) The contact force between the cycloidal gear and eccentric shaft, and (b) the contact force on input shaft in case A, B, and C.

more roller pins in contact and smaller maximum contact forces than case B, with a positive eccentric shaft deviation. However, the contact force does not directly affect the load-carrying capacity, and further analysis of the contact stress through the contact curvature needs to be considered.

In Fig. 12(b), although the maximum contact force is more significant in case B, its contact stress is smaller than in case C, which may be because case C has a smaller equivalent contact radius (the contact positions are slightly different from B).

In Fig. 13, the ideal case A also has more output pins in contact. Case B and C have almost the same output pin contact forces and stresses, which may be because they have the same parameters in output pins.

Fig. 14 reflects the contact force between the eccentric shaft $F_{ec,c}$ and the cycloidal gear, the contact force on input shaft $F_{e,c}$ as the eccentric shaft rotates from 0 to 2π in the three cases. $F_{e,c}$ and $F_{ec,c}$ are proportional and the analysis focuses on $F_{e,c}$, as Equation (47). In case B with positive eccentric shaft deviation, the contact force between the eccentric shaft and the cycloidal gear is the largest, and the fluctuation

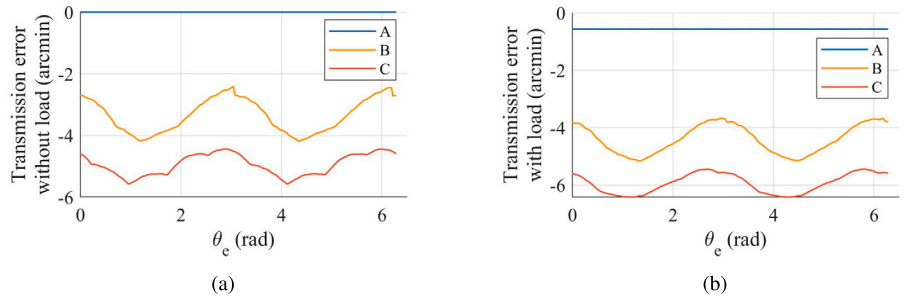


Fig. 15. (a) Transmission error under no-load conditions, and (b) transmission error under load conditions in case A, B, and C.

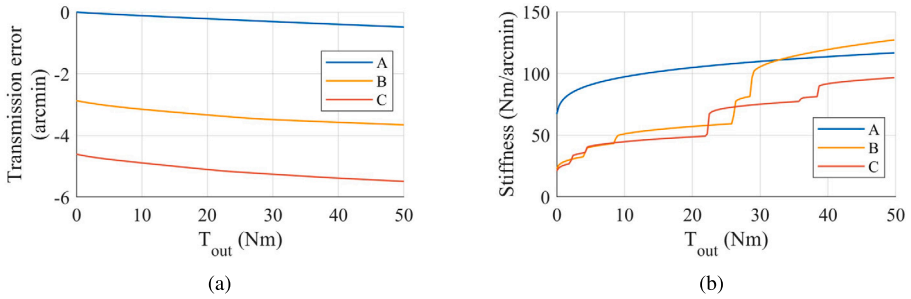


Fig. 16. (a) The transmission error with the external load when the eccentric shaft is locked, and (b) the transmission stiffness with the external load in case A, B, and C.

is the most severe, which may be related to the positions of roller pins in contact in case B, which bring a greater pressure Angle. Excessive eccentric shaft contact force is more likely to cause damage to the eccentric shaft bearing, which is also a basic form of damage in cycloidal drive.

In summary, the different deviations in the geometric parameters and clearance will decrease the load capacity of the cycloidal drive in different ways. The positive or negative deviations of the eccentric shaft significantly impact the load capacity, and the negative deviation shaft deviation is more beneficial for load capacity mainly related to the reduction of the equivalent contact radius.

4.1.2. The accuracy, backlash, and stiffness of the cycloidal drives in case A, B, and C

The transmission error can reflect the accuracy of a cycloidal drive. The transmission error is the difference between the actual output angle and the theoretical ideal output angle; the smaller the error, the higher the accuracy. Fig. 15 shows the transmission error of the cycloidal drive under the no-load ($T_{out} = 0$ Nm) and load ($T_{out} = 50$ Nm) condition for one revolution of eccentric shaft ($\theta_e \in [0, 2\pi]$) at counterclockwise speed $\omega_e = 200$ rad/s.

The transmission error under the no-load condition includes only the error generated by the clearance. Transmission error under the load condition has clearance error and additional deformation error. For the ideal case A, the transmission error without load is zero, and the transmission error with load fluctuates slightly. In the other cases with clearance, the gears are no longer perfectly meshed due to geometric parameter deviations. They exhibit significant transmission errors with fluctuations both with and without load.

It should be noted that the above error curves all exhibit the characteristics of overall offset and periodic fluctuation, where the overall offset mainly comes from the transmission lost motion, which significantly affects the absolute transmission accuracy. In contrast, the fluctuation reflects the relative accuracy.

The two non-ideal cases have similar relative accuracy, and the absolute transmission accuracy in case B with positive eccentric shaft deviations is better than that in case C.

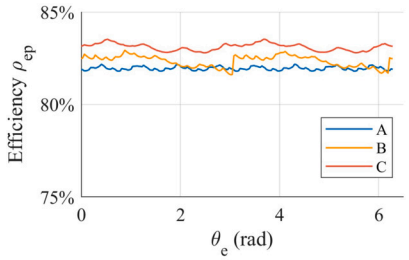


Fig. 17. Transmission efficiency in case A, B, and C.

Transmission backlash and stiffness are essential transmission performance indicators impacting transmission accuracy.

Fig. 16(a) shows the transmission error with the external load from 0 to 50 Nm when the eccentric shaft is locked. At an external load of 0, the transmission error here is the backlash. The transmission error will increase as the external load increases due to deformation. Backlash and deformation cause the lost motion problem, reducing absolute transmission accuracy and introducing unstable nonlinear effects into the robot joint servo system. Case B has a smaller backlash than case C, consistent with the results in Fig. 15.

Fig. 16(b) further shows the transmission stiffness for external loads from 0 to 50 Nm based on Fig. 16(a). It can be seen that the transmission stiffness of the cycloidal drive increases as the external load increases. There are abrupt changes in the transmission stiffness variation of the two non-ideal cases, possibly due to the increase in the number of contact points as the load increases.

Overall, the non-ideal case with clearance has a larger backlash and lower transmission stiffness than the ideal case. Positive eccentric shaft deviations have advantages in backlash compared to negative deviations.

4.1.3. The efficiency of the cycloidal drives in case A, B, and C

Transmission efficiency is essential for a cycloidal drive and is particularly important in highly dynamic robotic and flexible collaborative robot applications. Fig. 17 shows the variation of the transmission efficiency under the clockwise load $T_{out} = 60$ Nm and counterclockwise

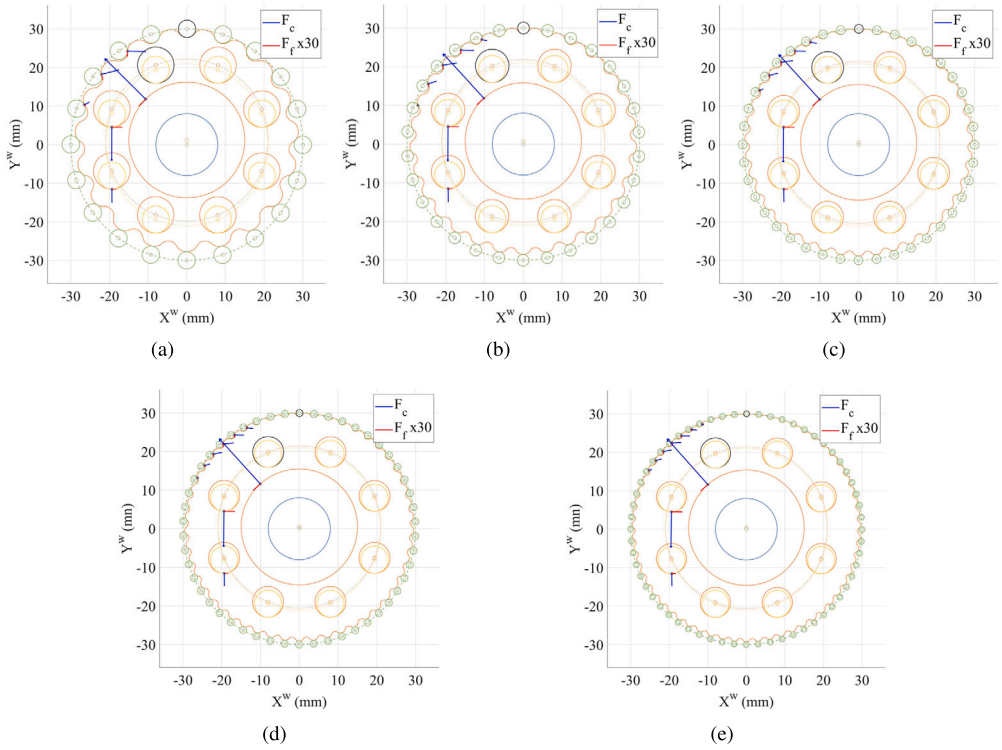


Fig. 18. Force state of the cycloidal gear in (a) $z_p = 20$, (b) $z_p = 30$, (c) $z_p = 40$, (d) $z_p = 50$, and (e) $z_p = 60$.

Table 2
Experimental parameters with different teeth numbers.

Parameters	Value				
Teeth number of pin gear z_p	20	30	40	50	60
Teeth number of cycloidal gear z_c	19	29	39	49	59
Ideal eccentric distance e (mm)	1.2	0.8	0.6	0.48	0.4
Ideal roller pin radius r_p (mm)	2.25	1.5	1.125	0.9	0.75
Ideal output pin-hole radius r_{wh} (mm)	4.7	4.3	4.1	3.98	3.9
Ideal roller pin distribution radius R_p (mm)	30				
Ideal output pin radius r_w (mm)	3.5				
Curtate coefficient K_1	0.8				

speed $\omega_e = 200$ rad/s condition for one revolution of eccentric shaft ($\theta_e \in [0, 2\pi]$).

The transmission efficiency varies at different eccentric shaft angles, and there are fluctuations in efficiency even in the ideal case A. As mentioned earlier, there is a transmission error even in case A from contact deformation, which is one of the reasons for the fluctuation of efficiency. In addition, the damping friction at the contact point is also one reason. Efficiency fluctuations introduce additional disturbing torque into the control of the robotics joint motors.

Comparing the three cases, case C has the highest efficiency, and case B has the lowest efficiency. The reason for this requires further analysis in Section 4.3.

4.2. Effects of teeth number of pin gear on cycloidal drive

For drives employed in robots, especially high dynamic robots, its transmission ratio is closely related to robot performance. For cycloidal drives, the transmission ratio and the teeth number of pin gear satisfy Equation (3). In this study, we use the CDFM to discuss the effect of the teeth number of pin gear, i.e., the transmission ratio on the cycloidal drive by simulation analysis, and provide recommendations for the selection of reduction ratio for application in robotics.

In this study, based on the case C simulation parameters, five different teeth number cases of $z_p = 20$, $z_p = 30$, $z_p = 40$, $z_p = 50$, and $z_p = 60$ were simulated. Meanwhile, to discuss the effect of teeth number more accurately individually, the same ideal roller pin distribution radius R_p, curtate coefficient K_1, and ideal output pin radius r_w are used for the five different tooth numbers of the cycloidal drive, and the ideal eccentric distances e are obtained by using K_1 according to the Equation (7), the ideal roller pin radiuses r_p were scaled by e. The ideal output pin-hole radius r_{wh} was obtained by e according to the Equation (1). The above parameters are organized into Table 2, and the other geometric and simulation parameters are consistent with case C. The force states of the cycloidal gears are shown in Fig. 18.

4.2.1. The load capacity of the cycloidal drives with different teeth numbers

Similarly, we analyzed the effect of z_p on the load capacity of cycloidal drives through the contact forces and contact stresses of the roller pins (Fig. 19) and output pins (Fig. 20), the contact force between the cycloidal gear and eccentric shaft, and the contact force on input shaft (Fig. 21) to analyze the effect of z_p on the load capacity of cycloidal drives.

The numbers of teeth in contact are different in cases with different z_p under loading. The larger z_p is, the more teeth are in contact, and the smaller the maximum contact force of the needle roller is. But since a large z_p leads to a smaller equivalent contact radius, the larger z_p is, the higher the maximum contact stress of the roller pin is.

Since the radius r_w and distribution radius R_w of the output pins are the same in five cases, the change of z_p has less effect on the con-

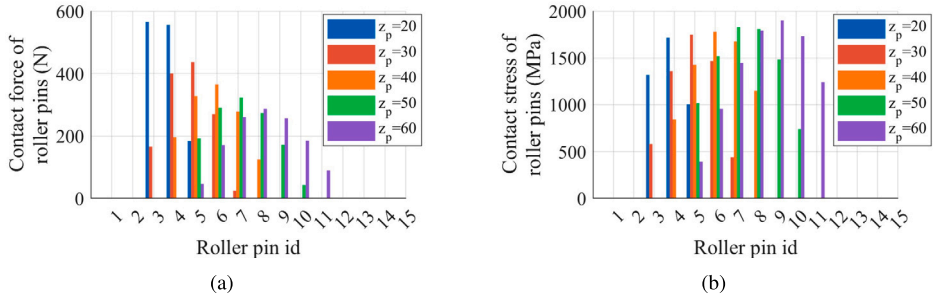


Fig. 19. (a) The contact forces of the roller pins, and (b) the contact stresses of the roller pins in cases with different teeth numbers.

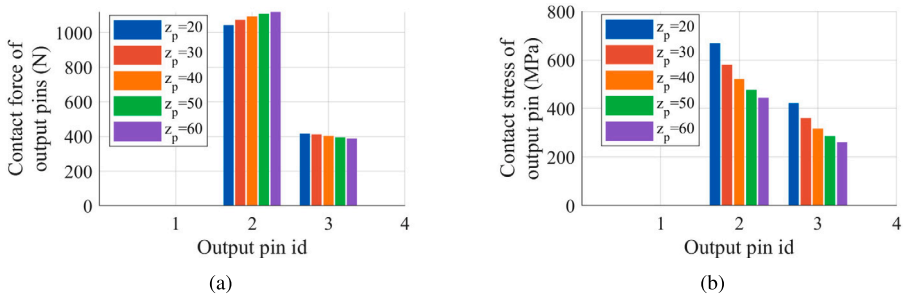


Fig. 20. (a) The contact forces of the output pins, and (b) the contact stresses of the output pins in cases with different teeth numbers.

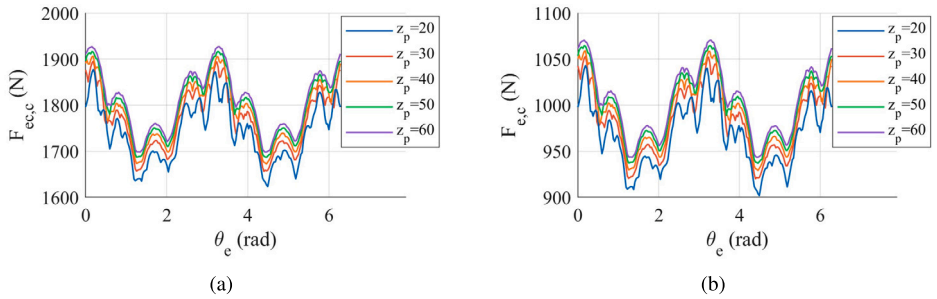


Fig. 21. (a) The contact force between the cycloidal gear and eccentric shaft, and (b) the contact force on input shaft in cases with different teeth numbers.

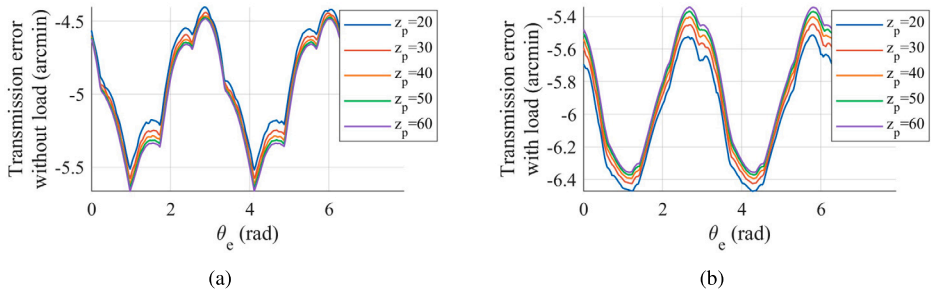


Fig. 22. (a) Transmission error under no-load conditions, and (b) transmission error under load conditions in cases with different teeth numbers.

tact force of the output pin. But the increase of e further leads to the decrease of the ideal output pin-hole radius r_{wh}. It increases the equivalent contact radius, decreasing the contact stresses of the output pins as z_p increases.

As z_p increases, the contact positions of the pin gear are slightly changed, which leads to a larger pressure angle and a larger contact force of the eccentric shaft and input shaft.

4.2.2. The accuracy, backlash and stiffness of the cycloidal drives with different teeth numbers

The no-load transmission error and load transmission error fluctuations do not change much as z_p increases with geometric deviations (Fig. 22(a)). However, since the change in z_p affects the position of the needle rollers involved in the contact, as z_p increases, its transmission lost motion increases, and the offset in the no-load error curve increases. The number of teeth in contact increases with z_p, which reduces the contact deformation, causing the transmission stiffness to increase with z_p (Fig. 23(b)). As the load increases, the number of teeth in contact increases, and the stiffness gradually increases. Although a large z_p leads to a larger lost motion, the transmission error is gradually smaller due to its better stiffness than that of a small z_p as the loading increases (Fig. 23(a)), which is reflected in (Fig. 22(b)), the offset of the load error curve decreases as z_p increases.

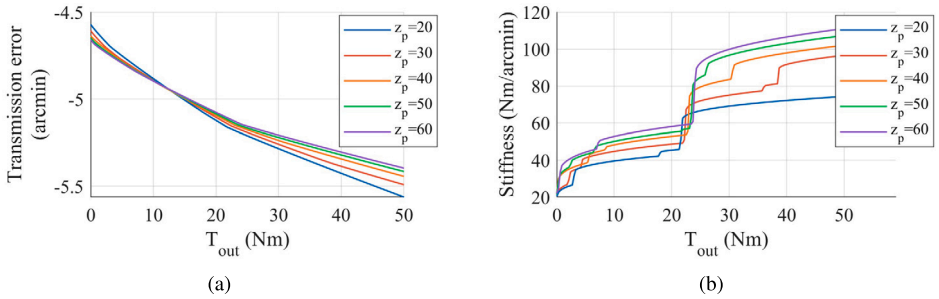


Fig. 23. (a) The transmission error with the external load when the eccentric shaft is locked, and (b) the transmission stiffness with the external load in cases with different teeth numbers.

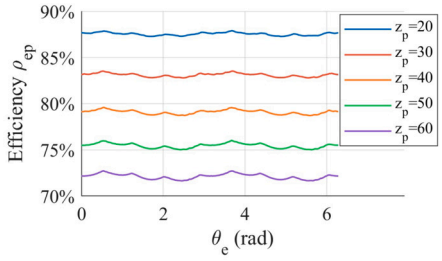


Fig. 24. Transmission efficiency in cases with different teeth numbers.

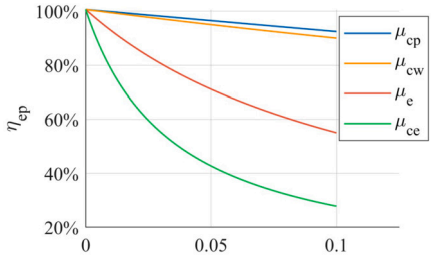


Fig. 25. Transmission efficiency in cases with different friction coefficients.

4.2.3. The efficiency of the cycloidal drives with different teeth numbers

As shown in Fig. 24, under the same friction and load conditions, the efficiency of the cycloidal transmission decreases significantly as z_p increases. In other words, increasing the transmission ratio will reduce efficiency significantly, which is consistent with the conclusion of our previous study [24]. This point needs to be emphasized in applying cycloidal drives in robotics, where the selection of the reduction ratio is closely related to the transmission efficiency (friction).

4.3. Effects of friction coefficients on the efficiency of cycloidal drive

The efficiency of a cycloidal drive is very important in practical applications. In the previous analysis, the effect of geometrical deviations and the number of teeth (transmission ratio) on the efficiency has been discussed. In the CDFM, four main types of friction are considered: the friction between pin gear and cycloidal gear, the friction between output pins and pin-holes, the friction between eccentric shaft and cycloidal gear, and the friction on input shaft. In this study, we discuss the impression of the four positional frictions on the overall efficiency by simulating the changes of friction coefficients μ_{cp}, μ_{cw}, μ_{ce}, and μ_e corresponding to the frictions mentioned above on the transmission efficiency. The degree of influence.

The simulation parameters for case C served again as the foundation for analyzing the transmission efficiency. Each of the friction coefficients μ_{cp}, μ_{cw}, μ_{ce}, and μ_e was individually chosen while setting the remaining friction coefficients and damping coefficients at 0. The simulation adjusted the selected friction coefficient incrementally from 0 to 0.1 in steps of 0.001 to get the corresponding efficiency. The resultant efficiency was calculated for $\theta_e = 0$.

Fig. 25 shows the variation of the transmission efficiency with the change of friction coefficients obtained by the above simulations. It is easy to understand that the transmission efficiency will decrease no matter which friction coefficient increases (friction increases). However, the effects of different friction coefficients on efficiency are significantly different. μ_{cp} and μ_{cw} have a minor effect on the transmission efficiency, and μ_{ce}, and μ_e exert a substantial effect on the efficiency, with μ_{ce} having the largest effect on the efficiency.

From Fig. 12(a), Fig. 13(a), Fig. 14(a), and Fig. 14(b), it can be seen that the eccentric shaft and input shaft have the more significant contact force in the cycloidal drive and also has the highest speed, which results high friction on it as well as a high friction power. Therefore, the friction on the eccentric shaft and input shaft has the more significant effect on the efficiency, especially the eccentric shaft, which also explains the difference in efficiency between the three cases in Section 4.1.3, where the crankshaft and input shaft forces are smaller in case C, so case C has higher efficiency.

4.4. Discussion

The numerical model method CDFM was used for the simulation experiments above, which considered the clearance, deformation, and friction in cycloidal drives.

We analyzed the effects of geometric deviations, teeth number (transmission ratio), and friction coefficients on cycloidal drives. The clearance caused by geometric deviations reduces the load capacity, accuracy, and stiffness of cycloidal drives but improves the transmission efficiency to some extent, in which the positive and negative eccentric deviations will have different effects on the performance. Under the same size, increasing the number of teeth will increase the maximum contact stress of the pin gear, increase the contact force on the eccentric shaft and input shaft, and increase the lost motion, but it will reduce the contact stress of output pins and improve the transmission stiffness. Increasing the number of teeth (transmission ratio) will significantly reduce the efficiency, which is very important. By analyzing the effects of different friction coefficients on efficiency, the study indicates that the friction with the most significant effect on efficiency comes from the eccentric shaft and input shaft. For the need to improve efficiency, we recommend increasing the appropriate clearance in cycloidal drives, reducing the transmission ratio of cycloidal drives, improving the lubrication, especially of the eccentric shaft and the input shaft, and designing to reduce the contact force between the eccentric shaft and the input shaft.

The simulation above reflects that many parameters influence the characteristics of the cycloidal drive, and a fast simulation method is necessary for cycloidal drive design. The CDFM uses the Levenberg-Marquardt algorithm to solve nonlinear equation groups. The PC used for calculation has an Intel i7-9750H CPU and 32 GB of memory. The solving time is related to the parameters of the cycloidal drive, such as the number of roller pins. For one given state, the average simulation time for "$z_p = 30$" is less than 3.5 s, and the average simulation time for

"$z_p = 60$" is less than 5.5 s. The faster simulation speed of the method is suitable for use in multi-parameter optimization design.

It should be noted that the simulation results in this study are mathematically valid. However, they may not directly and accurately correspond to the parameters of the actual cycloidal drive, which is because some physical constants need to be determined according to existing conditions, and the analysis ignores the influence of a small part of other factors, such as the bending deformation of the output pins. The friction coefficient and damping coefficient significantly impact the accuracy of efficiency analysis and must be correctly given based on actual lubrication conditions and friction forms. Accurate physical constants can improve the accuracy of predictions.

Although the prediction given by the method proposed in this study is not a perfect absolute performance prediction result, it can provide a relative prediction result that meets the needs of optimization design.

5. Conclusion

This paper proposes a numerical analysis method CDFM for designing and optimizing cycloidal drives used in high-dynamic robots. This method considers clearance, deformation, and friction to calculate the position of the contact point, contact friction force, contact force, and contact stress during the quasi-static transmission of cycloidal drives. The proposed method considers geometric parameter deviations, clearance, contact deformation, and contact friction to predict transmission accuracy, backlash, stiffness, and efficiency of the cycloidal drive.

Using the CDFM, the performance indicators of cycloidal drives with different parameters are simulated to analyze the effects of geometric deviations, teeth number (transmission ratio), and friction coefficients on cycloidal drives. The study shows that multiple parameters and parameter deviations influence cycloidal drives, and the proposed method provides good solution efficiency and is suitable for multi-parameter optimization design.

It is important to note that the method proposed in this paper enables relative performance prediction. However, obtaining accurate physical constants, such as friction coefficients, is necessary for accurate absolute performance prediction. Therefore, identifying physical constants through suitable design methods is essential for future research. Further development of the dynamic method based on the quasi-static model proposed in this paper is also important for future research.

Declaration of competing interest

The authors declare that they have no known competing financial interests or personal relationships that could have appeared to influence the work reported in this paper.

Acknowledgement

This work was supported in part by the Special Foundation of China Postdoctoral Science (Grant No. 2022T150161) and in part by the Self-Planned Task of State Key Laboratory of Robotics and System (HIT) (Grant SKLRS202301A02).

References

[1] P.L. García, S. Crispel, E. Saerens, T. Verstraten, D. Lefeber, Compact gearboxes for modern robotics: a review, Front. Robot. AI 7 (2020) 103, https://doi.org/10.3389/frobt.2020.00103.

[2] A.-D. Pham, H.-J. Ahn, High precision reducers for industrial robots driving 4th industrial revolution: state of arts, analysis, design, performance evaluation and perspective, Int. J. Precis. Eng. Manuf., Green Technol. 5 (4) (2018, 8) 519–533, https://doi.org/10.1007/s40684-018-0058-x.

[3] J.W. Sensinger, J.H. Lipsey, Cycloid vs. harmonic drives for use in high ratio, single stage robotic transmissions, in: ICRA IEEE International Conference on Robotics and Automation, IEEE, St. Paul, MN, USA, 2012, pp. 4130–4135.

[4] A.-D. Pham, H.-J. Ahn, Rigid precision reducers for machining industrial robots, Int. J. Precis. Eng. Manuf. 22 (8) (2021) 1469–1486, https://doi.org/10.1007/s12541-021-00552-8.

[5] A. Kakogawa, Y. Mori, T. Fukasawa, N. Kurimoto, S. Tokunaga, T. Tokuda, A. Yamamoto, S. Kawamura, A highly backdrivable robotic arm using low friction and high accuracy cycloidal geared motors: ALFHA, in: 2022 IEEE/SICE International Symposium on System Integration (SII), IEEE, Narvik, Norway, 2022, pp. 428–433.

[6] E. Saerens, S. Crispel, P.L. García, T. Verstraten, V. Ducastel, B. Vanderborght, D. Lefeber, Scaling laws for robotic transmissions, Mech. Mach. Theory 140 (2019) 601–621, https://doi.org/10.1016/j.mechmachtheory.2019.06.027.

[7] K. Lee, S. Hong, J.-H. Oh, Development of a lightweight and high-efficiency compact cycloidal reducer for legged robots, Int. J. Precis. Eng. Manuf. 21 (3) (2020) 415–425, https://doi.org/10.1007/s12541-019-00215-9.

[8] K. Wang, D. Marsh, R.P. Saputra, D. Chappell, Z. Jiang, A. Raut, B. Kon, P. Kormushev, Design and control of SLIDER: an ultra-lightweight, knee-less, low-cost bipedal walking robot, in: 2020 IEEE/RSJ International Conference on Intelligent Robots and Systems (IROS), IEEE, Las Vegas, NV, USA, 2020, pp. 3488–3495.

[9] J. Reher, E.A. Cousineau, A. Hereid, C.M. Hubicki, A.D. Ames, Realizing dynamic and efficient bipedal locomotion on the humanoid robot DURUS, in: 2016 IEEE International Conference on Robotics and Automation (ICRA), 2016, p. 8.

[10] T. Kim, K. Shi, K. Kong, A compact transmitted-force-sensing series elastic actuator with optimized planar torsional spring for exoskeletons, in: AIM IEEE/ASME International Conference on Advanced Intelligent Mechatronics (AIM), IEEE, Delft, Netherlands, 2021, pp. 572–577.

[11] J.-H. Shin, S.-M. Kwon, On the lobe profile design in a cycloid reducer using instant velocity center, Mech. Mach. Theory 41 (5) (2006) 596–616, https://doi.org/10.1016/j.mechmachtheory.2005.08.001.

[12] Y.-W. Hwang, C.-F. Hsieh, Geometry design and analysis for trochoidal-type speed reducers: with conjugate envelopes, Trans. Can. Soc. Mech. Eng. 30 (2) (2006) 261–278, https://doi.org/10.1139/tcsme-2006-0016.

[13] B. Chen, T. Fang, C. Li, S. Wang, Gear geometry of cycloid drives, Sci. China Ser. E, Technol. Sci. 51 (5) (2008) 598–610, https://doi.org/10.1007/s11431-008-0055-3.

[14] X. Sun, L. Han, K. Ma, L. Li, J. Wang, Lost motion analysis of CBR reducer, Mech. Mach. Theory 120 (2018) 89–106, https://doi.org/10.1016/j.mechmachtheory.2017.09.019.

[15] S. Malhotra, M. Parameswaran, Analysis of a cycloid speed reducer, Mech. Mach. Theory 18 (6) (1983) 491–499, https://doi.org/10.1016/0094-114X(83)90066-6.

[16] T. Mackic, M. Blagojevic, Z. Babic, N. Kostic, Influence of design parameters on cyclo drive efficiency, J. Balk. Tribol. Assoc. (2013) 12.

[17] W.-S. Lin, Y.-P. Shih, J.-J. Lee, Design of a two-stage cycloidal gear reducer with tooth modifications, Mech. Mach. Theory 79 (2014) 184–197, https://doi.org/10.1016/j.mechmachtheory.2014.04.009.

[18] X. Li, B.-k. Chen, Y.-w. Wang, T.C. Lim, Mesh stiffness calculation of cycloid-pin gear pair with tooth profile modification and eccentricity error, J. Cent. South Univ. 25 (7) (2018) 1717–1731, https://doi.org/10.1007/s11771-018-3863-z.

[19] X. Li, C. Li, Y. Wang, B. Chen, T.C. Lim, Analysis of a cycloid speed reducer considering tooth profile modification and clearance-fit output mechanism, J. Mech. Des. 139 (3) (2017) 033303, https://doi.org/10.1115/1.4035541.

[20] T.L. Tran, A.D. Pham, H.-J. Ahn, Lost motion analysis of one stage cycloid reducer considering tolerances, Int. J. Precis. Eng. Manuf. 17 (8) (2016) 1009–1016, https://doi.org/10.1007/s12541-016-0123-8.

[21] C.-H. Huang, S.-J. Tsai, A study on loaded tooth contact analysis of a cycloid planetary gear reducer considering friction and bearing roller stiffness, J. Adv. Mech. Des. Syst. Manuf. 11 (6) (2017) JAMDSM0077, https://doi.org/10.1299/jamdsm.2017jamdsm0077.

[22] A.-D. Pham, H.-J. Ahn, Efficiency analysis of a cycloid reducer considering tolerance, J. Frict. Wear 38 (6) (2017) 490–496, https://doi.org/10.3103/S1068366617060113.

[23] J.W. Sensinger, Unified approach to cycloid drive profile, stress, and efficiency optimization, J. Mech. Des. 132 (2) (2010) 024503, https://doi.org/10.1115/1.4000832.

[24] L. Qi, D. Yang, B. Cao, Z. Li, Y. Gu, Z. Xie, H. Liu, Prototype design and efficiency analysis of a novel robot drive based on 3 K-H-V topology, in: 2022 IEEE International Conference on Robotics and Biomimetics (ROBIO), IEEE, Jinghong, China, 2022, pp. 2249–2254.

[25] J.W. Sensinger, Efficiency of high-sensitivity gear trains, such as cycloid drives, J. Mech. Des. 135 (7) (2013) 071006, https://doi.org/10.1115/1.4024370.

[26] M. Matejić, M. Blagojević, N. Kostić, N. Petrović, N. Marjanović, Efficiency analysis of new two-stage cycloid drive concept, Tribol. Ind. 42 (2) (2020) 337–343, https://doi.org/10.24874/ti.880.05.20.06.

[27] M. Matejic, V. Goluza, M. Vasic, M. Blagojevic, Analysis of two-stage cycloid speed reducers dimensions and efficiency, in: M. Rackov, R. Mitrović, M. Čavić (Eds.), Machine and Industrial Design in Mechanical Engineering, vol. 109, Springer International Publishing, Cham, 2022, pp. 171–181.

[28] K.-S. Lin, K.-Y. Chan, J.-J. Lee, Kinematic error analysis and tolerance allocation of cycloidal gear reducers, Mech. Mach. Theory 124 (2018) 73–91, https://doi.org/10.1016/j.mechmachtheory.2017.12.028.

[29] H. Wang, Z.-Y. Shi, B. Yu, H. Xu, Transmission performance analysis of RV reducers influenced by profile modification and load, Appl. Sci. 9 (19) (2019) 4099, https://doi.org/10.3390/app9194099.

[30] Y. Wang, G. Liu, H. Yu, H. Mao, K. He, R. Du, Analysis of meshing characteristics of pins and pin housing integral structure in cycloidal planetary drive, in: IMECE ASME International Mechanical Engineering Congress and Exposition, American Society of Mechanical Engineers, Tampa, Florida, USA, 2017, V002T02A048.

[31] H.-J. Ahn, B.M. Choi, Y.H. Lee, A.-D. Pham, Impact analysis of tolerance and contact friction on a RV reducer using FE method, Int. J. Precis. Eng. Manuf. 22 (7) (2021) 1285–1292, https://doi.org/10.1007/s12541-021-00537-7.
[32] S.P. Radzevich, Theory of Gearing: Kinematics, Geometry, and Synthesis, second edition, CRC Press, Taylor & Francis Group, Boca Raton, 2018.
[33] K.L. Johnson, Contact Mechanics, Cambridge University Press, Cambridge [Cambridgeshire]; New York, 1985.